CERN/LHCC 96–38
LHC-B 96–10/LHCC 96–03
23 October 1996

Status and plan of R&D for the RICH detectors of LHC-B

The LHC-B Collaboration

Abstract

The particle identification system proposed for the LHC-B experiment is described, based on RICH detectors with three different radiator materials. The status of ongoing R&D is discussed, and a plan of future R&D is presented. The completion of this R&D plan should provide sufficient information for the preparation of a detailed design of the system.

Contents

1 Introduction

In this document, an R&D plan for the RICH detectors of LHC-B is presented. It has been written in response to a request from the LHCC, following the report made at the meeting of August 1996 [1]. The programme is described in detail and includes milestones, along with levels of effort at the participating institutions. Successful completion of the R&D described in this plan should provide the scientific basis for the preparation of the Technical Proposal for the RICH detector system; our aim is to be ready early in 1998. It updates and expands on the description of the overall R&D programme submitted previously [2, 1].

First a brief overview is given of the proposed RICH system, and the key issues requiring R&D are identified. Simulation of the system is described in Section 2, including studies of the expected resolution and of pattern recognition. In Section 3, the current status of the R&D programme is presented, including progress that has been made towards completion of the earlier goals defined in Ref. [2]. In Section 4 the plan for remaining R&D is described in detail, and finally the organization is discussed and milestones are specified.

1.1 Overview of proposed system

The requirements for particle identification in LHC-B have been determined from the momentum spectra of tracks from representative low- and high-multiplicity B decays. The low-multiplicity decays define the upper momentum limit required for π/K separation: in about 90% of simulated $B_d^0 \to \pi^+\pi^-$ decays neither track has momentum greater than 150 GeV/c in the very forward region ($10 < \theta < 120$ mrad), or greater than 65 GeV/c over the rest of the acceptance. The high-multiplicity decays define the lower momentum limit: in about 90% of simulated $B_s^0 \to D_s^- \pi^+\pi^+\pi^-$ decays (with a six-track final state) none of the tracks have momentum less than 1 GeV/c over the whole acceptance. Thus we aim to separate pions from kaons unambiguously over the momentum range $1 < p < 65$ GeV/c, and up to 150 GeV/c in the very forward region. These requirements can be met by RICH detectors, with three different radiator materials to cover different momentum regions: two gases (CF_4 and C_4F_{10}), and aerogel. Some properties of these materials (including aerogel with two different refractive indices) are listed in Table 1.

A description of the LHC-B spectrometer can be found in the Letter of Intent [3]. The region of approximately 2–7 m from the interaction point is occupied by a dipole magnet. For low-momentum tracks, particle identification must occur upstream of the dipole, before they are swept out of the acceptance. On the other hand, the very forward region is best instrumented downstream of the dipole, where the track separation is greater. The proposed system therefore has two RICH stations, with the CF_4 radiator (for high-momentum tracks) in a downstream station about 10 m from the interaction point. This detector is described in Ref. [3, 4], and features a gas radiator length of 1–2 m and a spherical focusing mirror with 12 m radius-of-curvature centred on the interaction point. A plane mirror is placed in front of the focusing mirror, inclined at 45° to bring the image out of the LHC-B acceptance, so that the photodetector material does not disturb the detectors that follow; the particle flux through the photodetectors is also substantially reduced.

The original design for the upstream station [3, 4] consisted of two consecutive de-

Material		CF_4	C_4F_{10}	Aerogel	
n		1.0005	1.0014	1.03	1.06
θ_c^{max}	[mrad]	30	53	240	340
$p_{thresh}(\pi)$	[GeV/c]	4.6	2.7	0.6	0.4
$p_{thresh}(K)$	[GeV/c]	16.3	9.4	2.0	1.4
$\sigma_\theta^{emission}$	[mrad]	0.1	0.6	0.3	0.5
$\sigma_\theta^{chromatic}$	[mrad]	0.3	0.6	1.2	1.7
σ_θ^{pixel}	[mrad]	0.2	0.5	0.5	0.5
σ_θ^{total}	[mrad]	0.4	1.0	1.4	1.9
N_{pe}		26	55	15	28
σ_θ^{track}	[mrad]	0.07	0.13	0.36	0.36
σ_β^{track}	[10^{-6}]	2	7	88	127
$p_{max}(3\sigma)$	[GeV/c]	146	73	20	17

Table 1: Some characteristics of the radiator materials proposed for the RICH system; the lower part lists the contributions to the resolution (from emission-point, chromatic and pixel errors), the total resolution per photoelectron, the mean number of detected photoelectrons in the ring image, the resolution per track on θ_c and β, and the upper limit of 3σ π/K separation for the proposed RICH detectors.

tectors, the first with aerogel radiator and the second with a high-index gas, and each with a geometry similar to that of the CF_4 detector. This had some disadvantages: as the aerogel was placed against the focusing mirror, any Cherenkov light produced had to traverse the full thickness of the aerogel before reaching the detector; this leads to a significant reduction of the number of photons, due to scattering. Secondly, the gas radiator length was constrained by the need to fit both the aerogel counter and angled mirror in the limited space between the vertex detector and the spectrometer magnet.

To avoid these drawbacks, a new geometry has been adopted for the upstream RICH station, which combines both aerogel and gas radiators in the same device, as illustrated in Fig. 1. The aerogel is moved up to the entrance window, so that light is now produced in transmission; the spherical focusing mirrors (one for each half of the detector, with 2 m radius of curvature) are tilted by about 200 mrad, to bring the image out of the acceptance; and the volume between the aerogel and mirrors is filled with C_4F_{10} gas. This is chosen due to its high refractive index and low dispersion; it is the heaviest fluorocarbon that remains gaseous at room temperature. As well as increasing the photon yield for both radiators, this layout has the advantage of almost halving the number of photodetectors required (as the same image plane is shared), and the amount of material is reduced as tracks pass through only a single mirror instead of four.

1.2 Key issues for R&D

1.2.1 Aerogel

Silica aerogel is a colloidal form of quartz, that is solid but very light. It has a long-established use in threshold Cherenkov counters, but the idea of using it for an imaging detector is recent [5], and has followed from the development of high quality, very clear, samples. Its attraction is that it can be produced with refractive index in the range

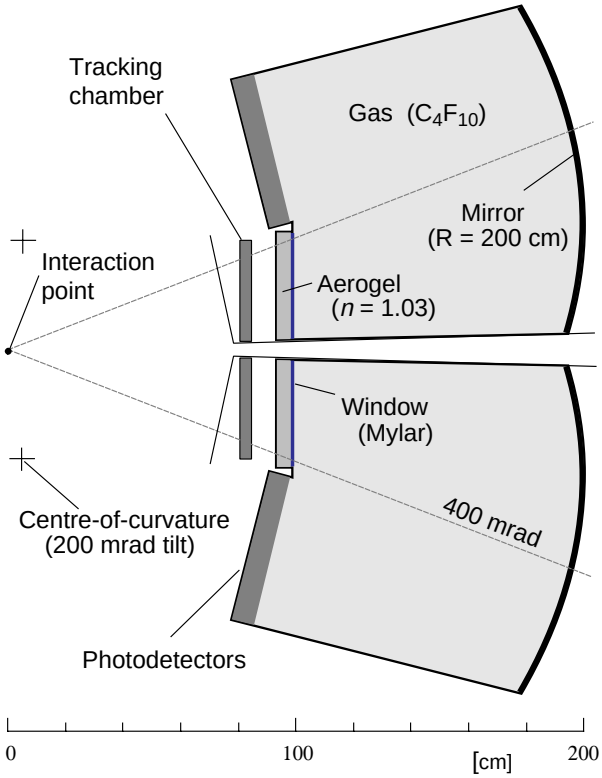

Figure 1: Layout of the new upstream RICH detector, seen from above (with the beam axis horizontal).

1.01–1.10, suitable for the low momentum end of the LHC-B particle identification requirements, otherwise only available with pressurized gas. One of the key issues for the R&D is to establish whether recent samples of aerogel are of suitable quality to be used as radiator material in a RICH.

The dominant cause of the scattering of light within aerogel is Rayleigh scattering, with the result that the transmission of light with wavelength λ through a block of thickness L is proportional to e^{-CL/λ^4}, where C is a coefficient that characterizes the clarity of the sample; recent samples have $C \sim 0.01\,\mu\mathrm{m}^4/\mathrm{cm}$, or even lower. This leads to 50% transmission for a 2 cm thick sample at about 400 nm, with little transmission below 300 nm. The scattered photons are expected to emerge at any angle, and will therefore lead to a randomly distributed background on the image plane. Taking into account the production of Cherenkov light by a particle traversing a sample of aerogel (uniform along its length), and the scattering of that light, the fraction of produced photons that will survive unscattered is given by $(1 - e^{-CL/\lambda^4})\lambda^4/CL$. Scattering dominates at short wavelengths, so a photodetector that is sensitive to visible light is required.

At its closest point, the aerogel will be positioned only a few centimetres from the beam, so its radiation hardness is important. This has been studied by a group from KEK, who observed no significant degradation of the properties of a sample of aerogel after irradiation up to 10 MRad equivalent dose [6].

1.2.2 Photodetectors

The requirements for the photodetectors of the RICH system are the following:

1. Single photoelectron sensitivity (for the aerogel high quantum efficiency is required in the visible);
2. Fast enough to cope with the time between bunch crossings of 25 ns;
3. Detector granularity $2 \times 2\,\mathrm{mm}^2$ ($4 \times 4\,\mathrm{mm}^2$ for the downstream detector);
4. Low noise;
5. Large area coverage $\sim 1.2\,\mathrm{m}^2$ ($2.6\,\mathrm{m}^2$ for the downstream detector), with highest possible active area.

Assuming that the devices are cylindrical with 11 cm diameter, the required area corresponds to 114 units (246 for the downstream detector). Hexagonal close-packing gives 90% coverage, and assuming an 80% active area within the device, this leads to 220,000 channels in the upstream detector (120,000 in the downstream). Low cost per channel is therefore important.

These requirements are not all met by any currently available detector, so this is a key area in which R&D is required. The main focus is on hybrid photodiodes (HPD's), which involve the electrostatic acceleration of electrons from a photocathode into a silicon detector [7]. Such devices are available commercially with a few pixels (and small active area), with a feed-through for each pixel out of the vacuum envelope; the main challenge is to increase the number of pixels per detector to $\mathcal{O}(1000)$, necessary to achieve the desired ratio of active to total area. In this case a feed-through per channel becomes impractical and it is necessary to include some electronics within the vacuum envelope. Two approaches are pursued: either strongly focussed, so that the photocathode is imaged onto a small detector with $\mathcal{O}(100\,\mu\mathrm{m})$ pixels, bump-bonded to a readout chip with matching pixel electronics; or gently focussed, onto a larger detector with $\mathcal{O}(1\,\mathrm{mm})$ pads, read out via conductive traces on the silicon surface to a separate electronics chip. The progress that has been made in the pursuit of these two approaches (denoted "pixel" and "pad" HPD's respectively) will be described in Section 3.

1.2.3 Backup solutions

Test-beam studies of aerogel, described below, have given very encouraging results, indicating that the background from scattered photons is low. Nevertheless, if this background is found to be unacceptable, then in the current design the aerogel can simply be removed from the upstream RICH, without compromising the performance of the rest of the system. In that case the lowest region of momentum for particle identification, below $3\,\mathrm{GeV}/c$, will be lost; between 3 and $9\,\mathrm{GeV}/c$ the C_4F_{10} radiator can be used in threshold mode, as pions will produce light but kaons will not. Detailed Monte Carlo studies are in progress to quantify the effect of such a change on the physics performance of the detector.

Concerning the photodetectors, commercially available HPD's already have suitable pixel size, low noise, high intrinsic speed and the required single photoelectron performance. They suffer, however, from low active area to total area ratio, and high cost. An alternative commercial solution is the multianode photomultiplier, available from Hamamatsu with up to 80 channels with $4\times4\,\mathrm{mm}^2$ segmentation. Such devices (with 16 channels and square packaging) have been selected by HERA-B for the instrumentation of their RICH detector. They also suffer from low active area, although HERA-B are attempting

to improve this with reflective light cones surrounding each pad. We are following these developments closely, although here again the cost per channel is currently high.

Multiwire chamber photodetectors, based on the photosensitive gas TEA with cathode pad readout, have been prototyped and tested in beams. Their response and speed are sufficient for LHC operation, but their energy band-pass (in the UV) only allows their use with the gas counters. The integrated quantum efficiency is a factor 2–3 lower than that achievable with HPD's, and would necessitate a longer radiator length.

Visible light photon counters (VLPC's) have recently been developed with extremely high quantum efficiency ($\sim$ 80% between 1.5 and 3 eV), using doped SiAs crystals operating at a temperature of 7 K. They represent a possible alternative technology that would work with the aerogel radiator. However, the need for liquid helium cooling would necessitate an optical fibre coupling between the RICH and photodetectors, with associated reduction in efficiency, and the cost is also currently high. We will follow closely the developments in this technology.

2 Simulation of the RICH system

2.1 Determination of expected resolution

Two critical issues had to be addressed for the new design of the upstream RICH: whether the shared image plane led to problems for the pattern recognition (discussed in Section 2.2), and whether the tilted mirror introduced unacceptable aberrations to the ring image. This was studied using ray tracing: for a given simulated track, photons are generated at fixed polar and azimuthal Cherenkov angles (θ_c, ϕ_c) along its length in the radiator. They are then reflected off the spherical mirror (initially aligned with centre-of-curvature at the interaction point), and their point of intersection found on a plane transverse to the beam axis. The position of this plane along the beam axis that minimizes the spread of impact points is then determined, and this is repeated for many azimuthal angles and many track impact points on the entrance window, to map the focal plane. The expected spherical focal surface is reproduced, with radius equal to half that of the mirror. When the mirror is tilted by 200 mrad the image moves out of the acceptance, as required, but the focal surface is no longer exactly spherical. For simplicity a planar photodetector surface is assumed, and the position of that plane is optimized to follow as closely as possible the focal surface: this leads to the angled detector plane visible in Fig. 1. The distribution of photon impact points on this plane, relative to their expected impact point for a perfectly imaging system, has an RMS of about 400 μm in both projections (for the C_4F_{10} radiator).

To express this resolution in terms of its effect on the reconstructed Cherenkov angle θ_c, which is the crucial issue for a RICH detector, it is necessary to determine the Cherenkov angles from the detected photon position and the assumed emission point (taken to be on the track, in the middle of the radiator). This is essentially the inverse of ray tracing, and is important as it also provides the starting point for pattern recognition studies described below. The required solution can be found in Ref. [8, 9].

Using this procedure, the contribution to the resolution on θ_c from the imperfect focusing of the tilted mirror (or equivalently, from the uncertainty on the photon emission point) is shown in Fig. 2 (a), with an RMS of 0.6 mrad. This is not a dominant contribution

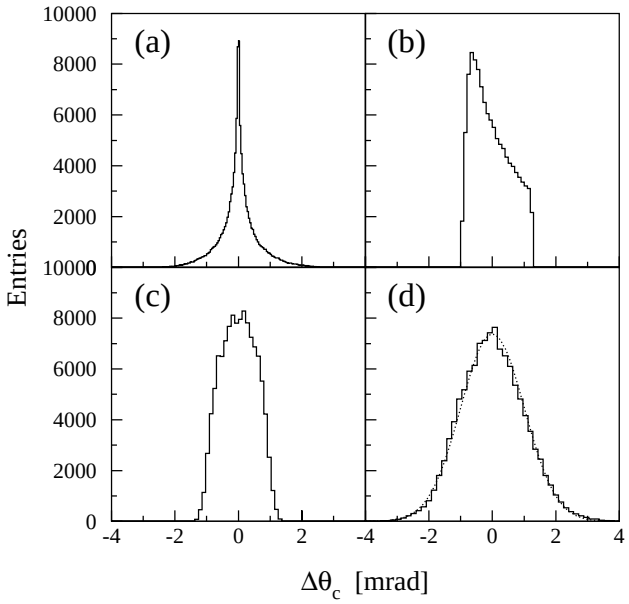

Figure 2: Contributions to the resolution of the C_4F_{10} gas RICH: (a) emission point uncertainty; (b) chromatic error; (c) pixel size; (d) overall resolution per detected photoelectron, with superimposed Gaussian fit.

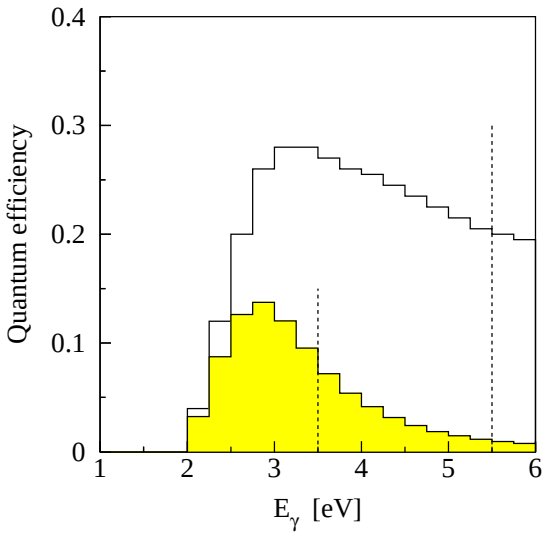

Figure 3: Quantum efficiency assumed for the photodetectors as a function of the incident photon energy; the effective quantum efficiency for a sample of aerogel is shaded, and dashed lines indicate the assumed window cut-offs.

to the resolution: there are also contributions from dispersion in the refractive index of the radiator, and from the finite pixel size of the photodetector. For C_4F_{10} the refractive index varies from 1.0013 at long wavelength, to 1.0015 at about 200 nm ($E_\gamma \approx 6$ eV). The energy dependence of the quantum efficiency assumed for the photodetectors is that of a typical bialkali photocathode, shown in Fig. 3. The entrance window of the photodetector will cut off the photon spectrum, and $E_\gamma < 5.5$ eV is assumed; this can be achieved with UV glass, avoiding the need for (expensive) quartz, and anyway extending to higher energies would increase the chromatic error. Taking account of the dispersion and assumed photodetector response, the resulting contribution to the smearing of the reconstructed Cherenkov angle is shown in Fig. 2 (b), with an RMS of 0.6 mrad.

The pixel size of the detector is then chosen to avoid limiting the resolution. The effect of a $2 \times 2\,\mathrm{mm}^2$ pixel is shown in Fig. 2 (c); it contributes 0.5 mrad to the resolution, and so is suitable. Including all three effects in the simulation, the overall resolution per photoelectron is shown in Fig. 2 (d), with a distribution that is close to Gaussian with an RMS of 1.0 mrad (for C_4F_{10}). The expected number of detected photoelectrons is given by [8]:

$$N_{\mathrm{pe}} = \frac{\alpha}{\hbar c} L \epsilon_A \int Q \mathcal{R} \sin^2\theta_{\mathrm{c}}\, dE_\gamma \ , \qquad (1)$$

where the first factor is a constant with value 370 $\mathrm{eV}^{-1}\mathrm{cm}^{-1}$, $L \approx 100$ cm is the radiator length, $\epsilon_A = 0.70$ is the assumed coverage of the photodetector active area, and $\mathcal{R} = 0.95$ is the assumed mirror reflectivity. Using the quantum efficiency Q from Fig. 3, this gives 50–60 photoelectrons/track (for a saturated ring, i.e. with $\theta_{\mathrm{c}} \approx \theta_{\mathrm{c}}^{\mathrm{max}}$), where the spread of values arises from the small change in radiator length over the acceptance. Thus the resolution per track is about 0.12 mrad (with a slight degradation at the limit of the

acceptance, to about 0.15 mrad, due to an increase in the emission-point contribution).

The contributions to the resolution have been determined for the aerogel radiator in the upstream RICH, in a similar manner to those for the gas radiator described above. For a thickness of 5 cm and clarity coefficient $C = 0.01\,\mu\mathrm{m}^4/\mathrm{cm}$, the effective quantum efficiency (i.e. the quantum efficiency scaled by the probability of no scattering, as a function of photon energy) is shown by the shaded distribution in Fig. 3. Scattering dominates at high energy, so a thin window (of mylar, or glass) will be placed after the aerogel in the upstream RICH detector, to absorb the (mostly scattered) photons with $E_\gamma > 3.5\,\mathrm{eV}$. This also serves to reduce the chromatic aberration, and separate the aerogel from the gas. For a track passing through 5 cm of aerogel with $n = 1.03$ the resulting number of detected photoelectrons in a saturated ring image is expected to be approximately 15, from Eq. (1), with an additional 5 or so scattered over the detector plane.

The results for the resolution are compared in the lower part of Table 1: the emission-point contribution is reduced (due to the smaller radiator thickness), the chromatic error is greater (due to the higher dispersion), and the pixel error is unchanged. The overall resolution per photoelectron is 1.4 mrad, which is reasonably well matched to the gas radiator resolution, permitting the use of common photodetectors. Also shown in the table are the equivalent figures for aerogel with a higher refractive index: the resolution per photoelectron is poorer, but this is offset by the larger number of photoelectrons per track, so the resolution per track on θ_c is unchanged. However, expressing the resolution in terms of the particle velocity β, which determines the particle-identification performance, the higher index sample gives a poorer σ_β, since $\sigma_\beta \approx \theta_c\,\sigma_\theta$ (for small θ_c); the $n = 1.03$ aerogel is therefore favoured, although the final choice will also depend on pattern-recognition considerations.

2.2 Pattern recognition studies

A typical simulated B event in the upstream RICH is shown in Fig. 4. Here the two detector planes are drawn side-by-side, and crosses mark the impact points of the reconstructed charged tracks in the event, extrapolated to the detectors as if they were reflected by the mirror. Dots mark the positions of detected photoelectron "hits" (assuming the quantum efficiency discussed above). Those originating from the C_4F_{10} gas radiator are visible as well-defined rings, of about 10 cm maximum diameter. The aerogel radiator leads to larger, more sparsely-populated rings, that are less obvious to the eye: one is picked out by circling its hits in the figure. There are also background hits from Rayleigh scattering in the aerogel, that are not associated to any ring. The event generator is PYTHIA, and a full GEANT treatment is used to provide track impact points on the entrance window of the RICH; a stand-alone routine is then used to simulate the Cherenkov light.

As can be seen for the gas radiator, the Cherenkov rings are not perfect circles, but are rather elliptical in shape, with a degree of distortion that depends on the direction of the track within the acceptance. Instead of attempting to fit directly these rings, a great simplification is achieved by reconstructing the Cherenkov angles at emission, (θ_c, ϕ_c), as described in Section 2.1. That calculation uses the hit position and the mirror parameters, and also the assumed photon emission point, which is taken to be on a track, half-way through the radiator; it is therefore made under the assumption that the hit originates from a given track. The hits which truly originate from that track will then all have the same value of polar Cherenkov angle $\theta_i = \theta_c$ (within the resolution), and have uniformly

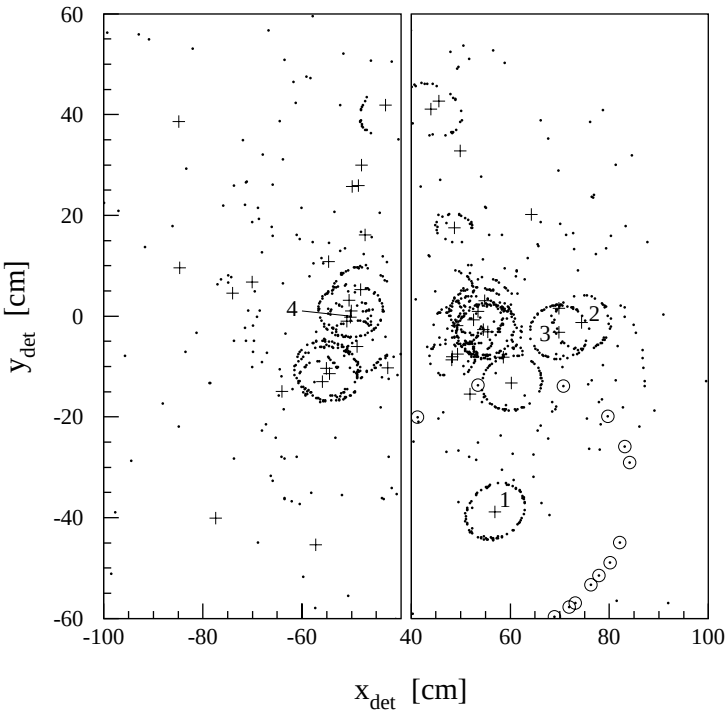

Figure 4: Display of the data from the upstream RICH for a typical simulated B event: the two detector planes are drawn side-by-side for clarity; the crosses represent the impact points of the charged tracks (if they were reflected in the mirror), four of which are labelled; hits on the aerogel ring image from Track 1 are circled for emphasis.

distributed azimuthal Cherenkov angle ϕ_i (where the subscript i denotes the assumption of parent track that has been made in calculating the angles).

This is illustrated in Fig. 5, where the Cherenkov angles (θ_2, ϕ_2) are reconstructed for the hits in the event of Fig. 4, assuming they originated from Track 2 (labelled in the figure). Those hits that really originate from Track 2 lie at constant θ_c, and are uniformly distributed in ϕ_c. The hits from neighbouring Track 3 describe a curling trajectory on this plot (whilst if (θ_3, ϕ_3) is plotted they fall at constant θ_c, and it is the hits from Track 2 that follow a similar curve).

The task of the pattern recognition is to identify such signals, even for tracks in the densely-populated regions of the event. An example is Track 4 in Fig. 4, for which the reconstructed θ_c plot is shown in Fig. 6(a). Most of the "background" to the signal of Track 4 (from the gas radiator) is in fact from the signals of other tracks. Two approaches to pattern recognition have been pursued:

1. Search for the most significant peak. For each track the θ_i histogram is filled, and a window is opened ($\pm 2\,\sigma_\theta$) around the expected θ_c for each of the possible mass-hypotheses (e, μ, π, K, p). The number of entries within the window is counted, the background estimated from the side-bands, and the signal significance calculated. The most significant peak is selected, amongst all combinations of track and mass-hypothesis; the hits within that peak are flagged as assigned (and are not used in subsequent iterations), and the procedure is repeated for the remaining tracks. In the event illustrated, Track 1 has the most significant peak (under the e hypothesis), whilst Track 4 has one of the lower significances; it is still, however,

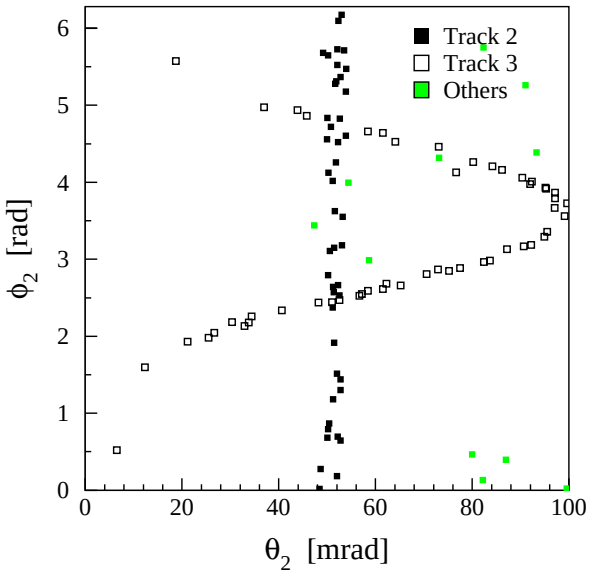

Figure 5: Reconstructed Cherenkov angles ϕ_c vs. θ_c for hits in the event of Fig. 4, assuming that they originate from Track 2; the true origin of the hits is indicated by shading.

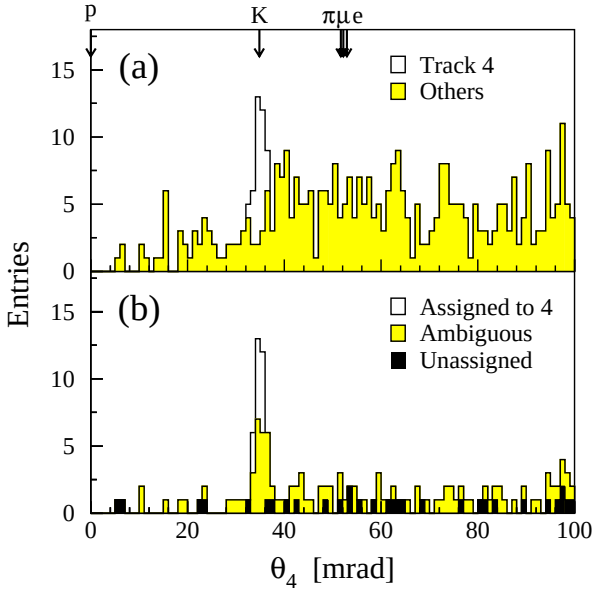

Figure 6: Reconstructed Cherenkov angle θ_c for hits in the event of Fig. 4: (a) assuming that the hits originate from Track 4; (b) after removing the hits unambiguously assigned to other tracks.

correctly identified (as a kaon), as are all tracks in the event. Removing the hits that have been unambiguously assigned to other tracks, the peak in the plot of θ_4 becomes much cleaner, as shown in Fig. 6 (b). However, fitting such resulting θ_i distributions is no longer useful as they are biassed by the $\pm 2\,\sigma$ cut that has already been applied. This is the motivation for the alternative approach, a global fit:

2. Simultaneously fit for θ_i of all tracks. A χ^2 is calculated that the detected hits originate from the set of tracks, each with a given assumed θ_i; the hits are assigned to the nearest track image (i.e. to the track i that minimizes $|\theta_{\rm hit} - \theta_i|$). Then:

$$\chi^2 = \sum_{\rm hit} \frac{(\theta_{\rm hit} - \theta_i)^2}{\sigma_\theta^2} + \sum_{\rm track} \frac{(n_{\rm assign} - n_{\rm expect})^2}{n_{\rm expect}} \ , \qquad (2)$$

where $n_{\rm assign}$ is the number of hits assigned to a track, and $n_{\rm expect}$ is the number expected (from Eq. (1)). To this χ^2 a term is added for the flatness of the ϕ_i distributions, calculated from histograms of $\Delta\phi$ (the difference in ϕ_i for each pair of hits associated to a track) which are flat if the hits are truly from the same track. The χ^2 is then minimized with respect to all θ_i. For the event shown all tracks have their Cherenkov angle correctly reconstructed (within errors).

The global approach looks promising; its extension to include the aerogel hits (with their poorer signal/background) is underway.

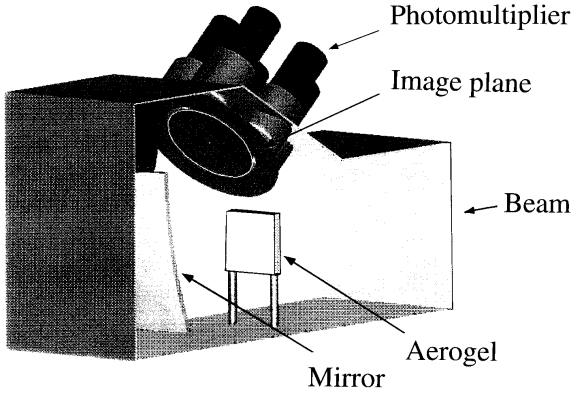

Figure 7: Apparatus used for the aerogel beam test; (for the test described, the illustrated photomultipliers were replaced by a one-inch tube, mounted on a motorized stage).

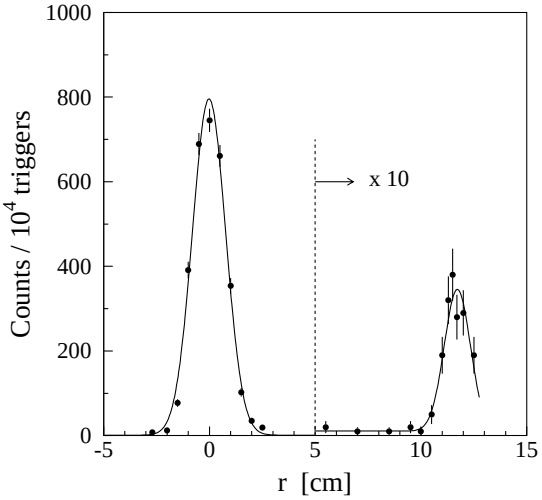

Figure 8: Number of photomultiplier counts as a function of the position of the photomultiplier across the image plane; the peak around $r = 0$ is from the nitrogen ring, the other is from the aerogel.

3 Status of R&D

3.1 Aerogel

3.1.1 Procurement of samples

Samples of aerogel have been procured from KEK ($n = 1.03$ and 1.02), JPL ($n = 1.01$ and 1.03), Air Glass ($n = 1.025$ and 1.06) and LLNL ($n = 1.15$). In addition, our Belle (KEK) colleagues have sent us new samples of their best production ($12 \times 10 \times 2.5\,\mathrm{cm}^3$ in size with index $n = 1.03$). We proceeded directly to test beam measurements of the properties of these samples.

3.1.2 Aerogel beam tests

Beam tests were performed this summer at CERN, by LHC-B in collaboration with groups from Bari, Lecce and Rome (Sanità)[1]. The apparatus used is illustrated in Fig. 7: it consists of a light-tight box, flushed with nitrogen, containing an angled spherical mirror (of 90 cm radius-of-curvature) with a sample of aerogel supported in front; a one-inch photomultiplier mounted on a motorized stage is arranged so that it can scan horizontally across the focal plane of the mirror. This setup has been exposed to a 10 GeV π^- beam from the PS. The first results were obtained using a 3 cm thick sample of aerogel produced at KEK, with nominal refractive index $n = 1.029$ and measured clarity $C = 0.01\,\mu\mathrm{m}^4/\mathrm{cm}$.

The passage of pions through the nitrogen gas generates Cherenkov light at small angle (~ 20 mrad), leading to a ring on the focal plane that is not resolved by the photomultiplier. A threshold was applied to the photomultiplier output to suppress noise but maintain sensitivity to single photoelectrons, and it was then scanned across the image

[1]These groups are planning to use aerogel in an upgrade of the HERMES experiment at DESY; their help in providing and setting up the detector is gratefully acknowledged.

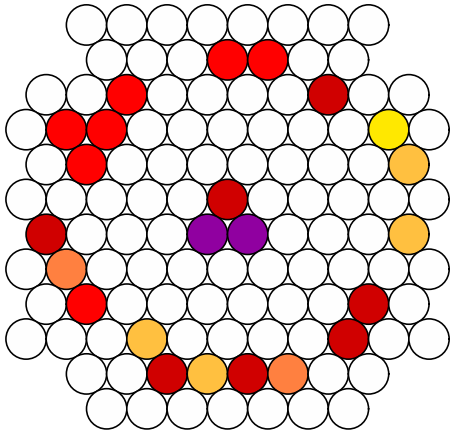

Figure 9: Event display from the aerogel beam-test with an array of one-inch photomultipliers; the density of shading indicates the pulse height.

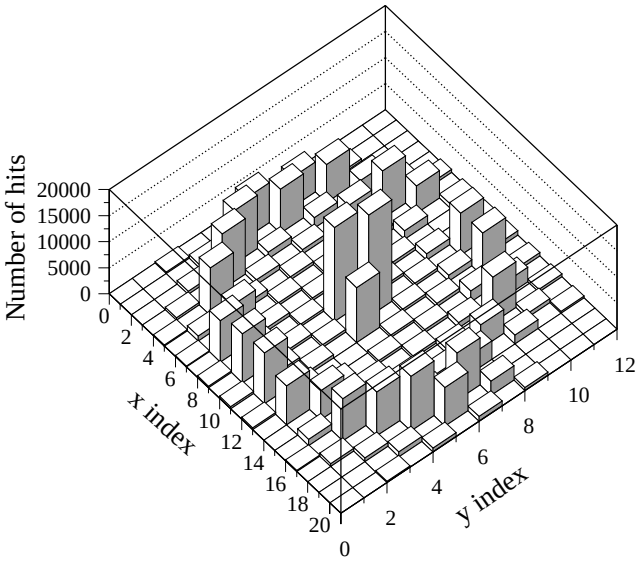

Figure 10: Distribution over the image plane of the number of hits in each photomultiplier, summing an entire run (of 30,000 events).

plane. The variation of the number of counts (per 10^4 triggers) with position r is shown in Fig. 8, where the origin of position has been chosen to lie at the centre of the strong nitrogen signal. A clear peak is seen in the count rate at $r = 11.6\,\mathrm{cm}$, corresponding to the Cherenkov ring image from the aerogel (the same enhancement was also seen when the scan was made in the opposite direction); the width of the peak is dominated by the size of the photomultiplier. Given the focal length of the mirror, this radius corresponds to a refractive index of 1.03, consistent with its nominal value. The background count rate, between the aerogel and nitrogen peaks, is very low, as expected for the high clarity aerogel sample.

The fraction of events f_0 which have no signal when the photomultiplier is sitting on the aerogel peak can be determined from a comparison of the photomultiplier pulse-height distributions, when on the aerogel peak or in the background region; a value of 0.70 is found. For a Poisson distribution, $f_0 = \mathrm{e}^{-\mu}$, where μ is the mean number of photoelectrons detected within the photomultiplier acceptance; thus $\mu = 0.35$. Scaling by the ratio of the aerogel ring circumference to the photomultiplier diameter, this corresponds to about 14 detected photoelectrons per track, which is in good agreement with the expectation.[2] A summary of these results will shortly be submitted for publication.

In a second phase of the beam test, the single photomultiplier was replaced by an array of 114 one-inch photomultipliers, close-packed to cover the image plane.[3] An example of an event display achieved with this array is shown in Fig. 9. Applying a threshold to the photomultipliers to separate the photoelectron signals from pedestal, and summing over a run of 30,000 events, the distribution over the image plane of the number of hits in each photomultiplier is shown in Fig. 10. The ring produced by the aerogel is strikingly visible,

[2] The prediction of 15 detected photoelectrons given earlier was for a thicker sample (5 cm), but only 70% detector coverage was assumed.

[3] We are grateful to our colleagues from BaBar (SLAC) for the loan of these photomultipliers.

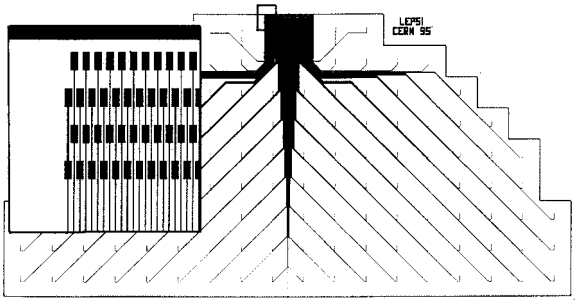

Figure 11: Layout of a silicon pad detector: the tree-like structure visible is the fan-in to the electronics chip, which is wire-bonded to the upper edge; the insert shows the region of the bond pads.

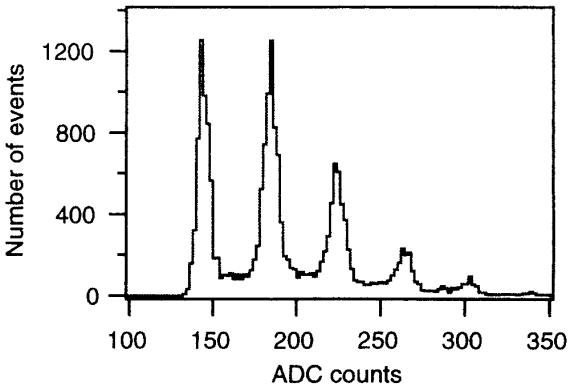

Figure 12: Pulse-height spectrum from a single pad of the silicon detector, when mounted in the HPD test setup; the leftmost peak is the pedestal, the others show the clearly resolved photoelectron signals.

whilst an enhancement is seen in the central three photomultipliers from light produced in the nitrogen. Once again, the low level of background hits between the nitrogen and aerogel signals testifies to the high clarity of the sample used. Similar data has been taken for a variety of different samples of aerogel, scanning over the surface of individual samples, and stacking them to obtain thicknesses between 2 and 8 cm. A paper reporting the final results of this study is in preparation, including the refractive indices and clarity coefficients measured, and the uniformity observed.

3.2 Pad HPD

The approach to HPD design using gentle focussing onto a pad detector is described in detail in Ref. [10]. Silicon half-wafers implanted with 128 $4 \times 4\,\mathrm{mm}^2$ pads have been produced, with the layout shown in Fig. 11. The fan-in brings the signals to the edge of the wafer, where they are connected to a Viking/VA2 readout chip (with 128 channels, and $\sim 1\,\mu$s peaking time) by wire bonding. These detectors were received from the foundry in January 1996. Leakage current and capacitances were measured and found to be within specifications: 60 nA/128 pads at full depletion voltage of 85 V, corresponding to less than 0.5 nA/pad, and each pad had a capacitance to other pads of 6.3 pF and to the backplane of 3.2 pF. The characterization of the detectors is complete and we are confident that the characteristics of future wafers can be reliably predicted.

Pairs of these detectors have been mounted in an optical test chamber, as proposed in Ref. [2]. The chamber is continuously pumped for vacuum, with a CsI photocathode and 15.7 kV accelerating voltage, and is illuminated with a collimated light source. It was delivered and assembled in April–May 1996 and has served to characterize the response of the silicon detectors to accelerated photoelectrons. A typical pulse-height spectrum achieved is shown in Fig. 12, demonstrating the low noise ($\sim 300\,e^-$ ENC) and showing the cleanly separated photoelectron peaks. With a 3σ cut on the pedestal we have achieved 96% single-electron efficiency. The single photoelectron signal was $4100\,e^-$ at 15.7 kV acceleration voltage, thus S/N $\approx$ 15 in accordance with expectations. It was found that when hitting the centre of a $4 \times 4\,\mathrm{mm}^2$ pad with a $1\,\mathrm{mm}^2$ beam only 1.3% of nearby

pads fired, indicating that the probability of backscattered photoelectrons re-entering the detector is suitably low. Charge sharing due to drift diffusion was found to occur only in a 10 μm region at the pad edge, so even for a 1 mm^2 pad this would amount to just a 4% effect. It will be reduced by a factor of ~ 2 for 200 μm thick silicon rather than the 500 μm thick wafer now used. A paper has been written describing these results, and is appended to this report [10].

3.3 Pixel HPD

The alternative approach to HPD design, using stronger focussing onto a pixel detector, is represented by the "Imaging Silicon Pixel Array" (ISPA tube), for which a prototype exists with 1024 pixels of $500 \times 75\ \mu$m^2, and an 18 mm diameter photocathode [11]. It was produced by an RD-7/LAA collaboration, using pixel electronics developed by RD-19 [12], that was encapsulated in a vacuum envelope by DEP (Delft Electronic Products, Roden, NL).

3.3.1 Detection efficiency

The efficiency of detection of a hybrid silicon pixel array tube can be described by the quantum efficiency (QE) of its photocathode and its overall detection quantum efficiency (DQE). The QE corresponds to the ability for a given photocathode to release one photoelectron when hit by a photon. For an ISPA tube equipped with a quartz window and a UV-enhanced photocathode, the QE (measured by DEP) exceeds 25% between 200 and 360 nm, and 20% at 440 nm. (These values are not optimized and can still be improved.) The DQE results from the effective efficiency $E_{\rm eff}$ with which one photoelectron is finally detected by the silicon detector and its associated electronics; the DQE is thus equal to QE multiplied by $E_{\rm eff}$. In the case of ISPA tubes, the front-end electronics (developed by the RD-19 collaboration for charged particle tracking) is binary and comprises a fast charge preamplifier (less than 100 ns shaping time), a comparator with adjustable threshold, a delay line, a coincidence logic and a memory element. Optimization of the performance of this electronics is a trade-off between noise, spatial precision, readout speed and power consumption. A phenomenon inherent to any kind of hybrid photon detector has also to be considered: the photoelectrons have a 20% probability to be backscattered at the surface of the silicon detector, releasing a charge signal ranging from zero to a maximum given by the acceleration voltage. Consequently, the key parameters for good detection efficiency are the charge signal amplitude released by one photoelectron in the pixel detector and the comparator threshold of the pixel binary electronics.

The single-photoelectron efficiency of the first generation ISPA tube was recently measured [13] using a low-intensity LED. The resulting pulse-height spectrum can be seen in Fig. 13, where the signal from a global analogue output is shown, from the backplane of the silicon. $E_{\rm eff}$ is determined by counting the number of fired pixels as a function of the tube high voltage, as shown in Fig. 14. It starts to increase from zero above 10 kV, has a maximum gradient at 18.5 kV and reaches 71% at 27 kV (the maximum potential allowed by the tube design). The 29% loss is attributed to photoelectrons backscattered in the silicon detector, or detected at the pixel boundaries (charge sharing), which release a charge signal too low to exceed the comparator threshold of the pixel electronics. Higher $E_{\rm eff}$ values are expected from the use of improved electronics with lower comparator thresh-

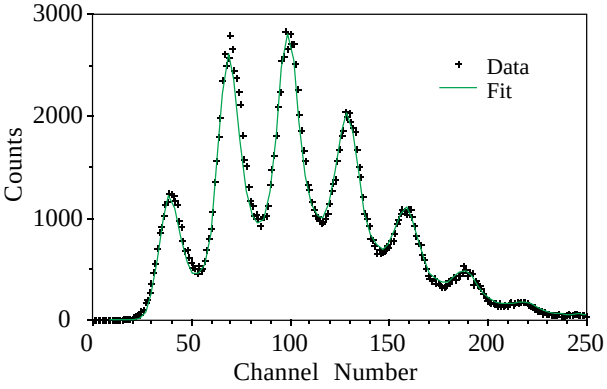

Figure 13: Pulse-height spectrum from the global-analogue output of the ISPA tube, illuminated with a low-intensity LED; (this signal is taken from the backplane, so the capacitance is greater than that of individual pixels).

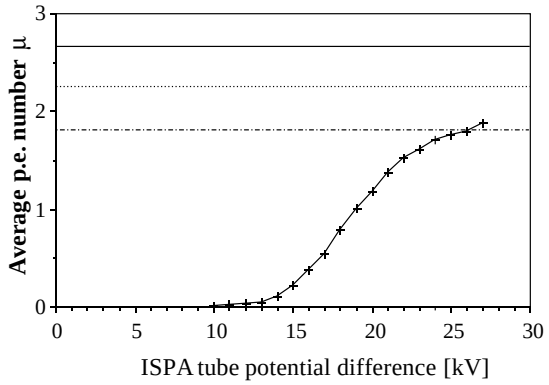

Figure 14: Average number of fired pixels per event for the ISPA tube, when illuminated as in Fig. 13, as a function of the applied high voltage; the lines indicate the limit for full efficiency (2.7 hits/event) and the reduction due to charge sharing, and backscattering.

old (see below) and thinner silicon detectors reverse-biased at higher voltages in order to reduce charge-sharing effects.

3.3.2 B-field effects

The new ISPA tube designs are based on standard image intensifier geometries with electrostatic demagnification by a factor of 4 to 5. In order to study how these geometries are sensitive to the expected stray field of the LHC-B dipole magnet (which has a simulated maximum value of 36 Gauss in the HPD detector plane of the upstream RICH), some tests have been performed with a standard 18:7 mm image intensifier (i.e. a cross-focussed model with cathode and anode active diameters 18 mm and 7 mm respectively) [14]. An optical test pattern was projected onto the tube input window, and the output image read out by a CCD. The results can be summarized as follows: with a magnetic field transverse to the tube axis, no image rotation occurs and a slight image distortion is visible (less than 500 μm in terms of input plane coordinates). With a longitudinal field, an image rotation is observed and the distortion is bigger. However, it still does not exceed 500 μm (after image rotation corrections). These first results, obtained with an unshielded tube, seem promising and the use of such demagnifying geometries can be envisaged. Very thin magnetic shields made of mu-metal are under study.

4 Planned R&D

4.1 Aerogel

Here most of the tests that had been foreseen have now been performed, although the analysis of the test beam results has still to be completed. We intend to measure the clarity of further samples when they become available, and will investigate whether baking the aerogel improves its properties.

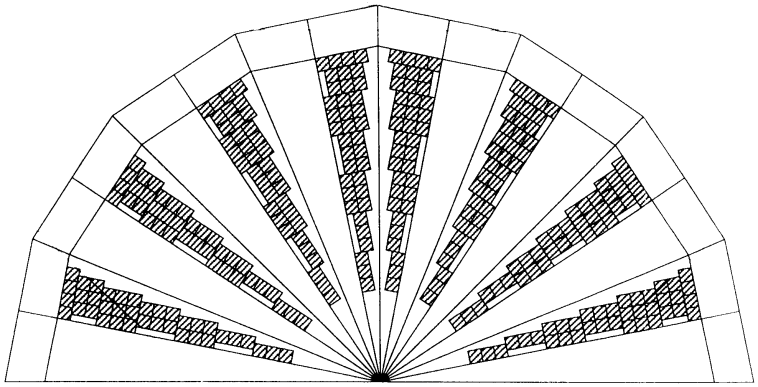

Figure 15: Layout of half of the 2048-pad detector design on a silicon wafer, with some of the $1 \times 1\,\mathrm{mm}^2$ pads shown shaded.

One further test that is planned is to study the intrinsic spatial resolution of the aerogel ring image, with a higher-precision detector than the 25 mm diameter photomultipliers used so far: one possibility is to mask a narrow entrance slit on the photomultiplier before scanning the image as before.

4.2 Pad HPD

The next step for the pad HPD development is to use smaller pads, and encapsulate the detector in a glass tube under vacuum.

4.2.1 Silicon detectors

A detector with 484 pads of $1.3 \times 1.3\,\mathrm{mm}^2$ is just now (October 1996) starting lab tests. Signals have been seen and no special difficulties encountered with the reduced pad size. Readout is obtained through four 128-channel Viking/VA3 chips with a noise level ($\sigma = 200\ e^-$) even lower than the VA2.

The design for a detector with 2048 pads of $1 \times 1\,\mathrm{mm}^2$ is complete, and orders have been placed for a 23 detectors. Besides having a reduced pad size, these detectors will have two new features: AC coupling and 200 μm thickness. Delivery is expected by early 1997. First tests of the 2048-pad device will use 16 VA3 chips of 128 channels, but later we will use the new SCT chip with 25 ns peaking time (see below). The layout of a half detector on the silicon wafer is shown in Fig. 15; it has 50 mm active diameter, with the readout chips and multiplexing bus lines on the periphery. For LHC-B we require a photodetector granularity of $2 \times 2\,\mathrm{mm}^2$ for the upstream RICH and $4 \times 4\,\mathrm{mm}^2$ for the downstream. With the chosen demagnification factor ($\times 2$), this will require detectors with 1×1 and $2 \times 2\,\mathrm{mm}^2$ pads, respectively; hence a 110 mm diameter HPD (with 100 mm photocathode) will contain either 2048 or 512 pads. The 512-pad detector will have the same sensitive diameter as the 2048-pad detector, with larger pads that can be read out with 4 (rather than 16) 128-channel chips.

4.2.2 Read-out electronics

The Viking/VA2 chip was originally developed to read out silicon strip detectors. We have used this chip in the first stages of the R&D effort because it is known, tested and

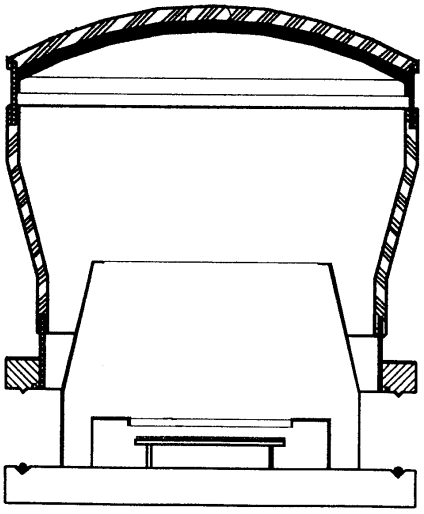

Figure 16: Cross-section through the glass envelope for the pad HPD: it is shown in position above the base-plate, which holds the silicon detector and focussing electrodes.

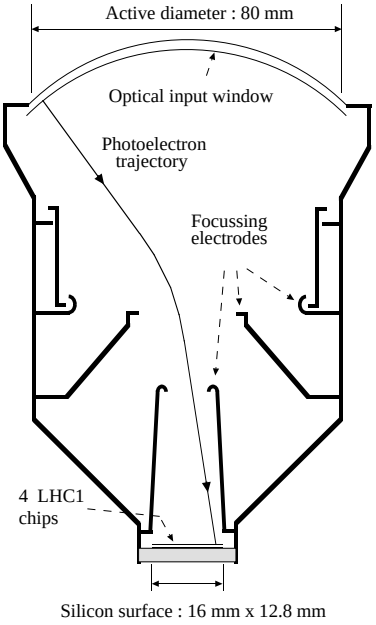

Figure 17: Schematic design of the large pixel HPD: the focussing electrodes give substantial demagnification onto the silicon detector, composed of four LHC1 chips in a rectangular array.

reliable; however, with $\sim 1\,\mu$s peaking time, it is much too slow for operation at LHC.

The CERN group of P. Weilhammer has been developing a fast SCT chip (25 ns peaking time) for ATLAS. They are also designing the SCT-128 chip for use with our HPD designs (4 chips will be required for the 512-pad HPD, 16 chips for the 2048-pad HPD). A noise level of 350 e^- is calculated for the chip, and preliminary measurements support this estimate. A paper with first results from an SCT chip prototype is now available and is appended to this document [15].

4.2.3 Facility for "in-house" HPD production

A suitable glass envelope has been designed for the pad HPD, with a UV glass window of 11 cm diameter, as illustrated in Fig. 16. Four of these glass envelopes have been ordered and should be received soon for first tests. The transparency of the UV glass window allows photon detection up to 5.5 eV as required for the gas RICH detectors.

The visible-light photocathode deposition apparatus has been designed, with facility for making a high vacuum seal between the glass envelope and base-plate, as shown in Fig. 18. The glass envelope is visible in the figure towards the top of the apparatus, above a hydraulic press that will be used in the sealing of the tube: the knife-edge on a stainless steel flange at the bottom of the envelope will be pressed into an indium filled groove in the base-plate, at room temperature. The apparatus is designed for a vacuum level of 10^{-10} mbar, with individual dispensers of Sb, Cs and K, and facility for on-line monitoring of quantum efficiency. We have started ordering and fabricating components and expect to start assembly of the apparatus in Spring 1997.

In parallel with this development, we will investigate the possibly of encapsulation by industry.

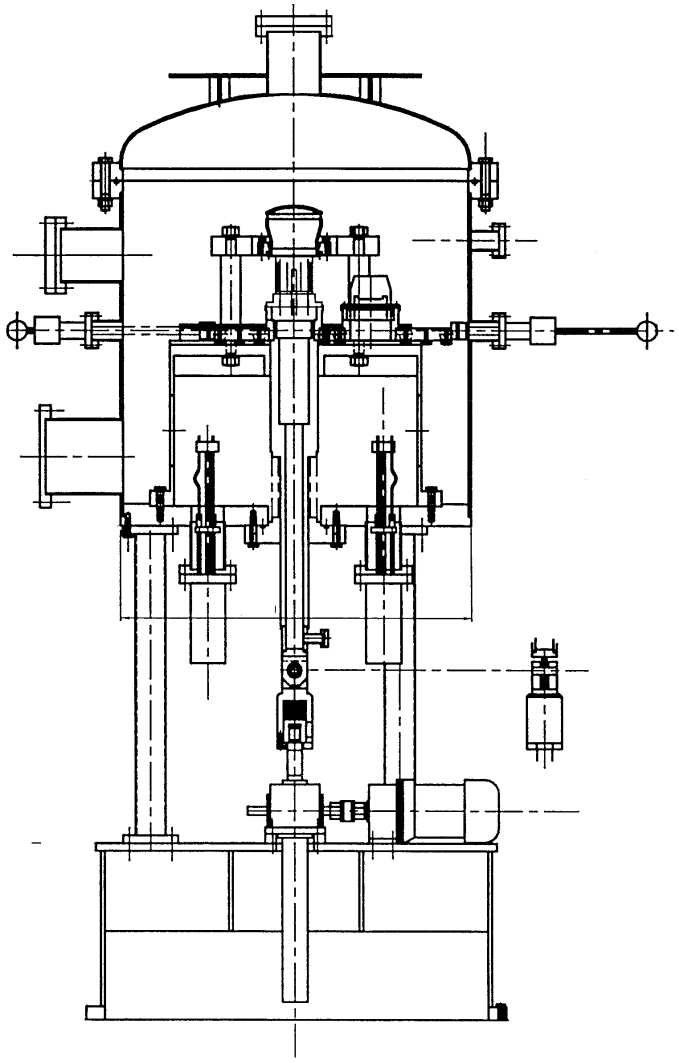

Figure 18: Design of the apparatus for encapsulation of the silicon pad detectors inside a glass envelope, under high vacuum, with facility for photocathode deposition and control; the unit is 2 m in height.

4.3 Pixel HPD

A new pixel detector chip (LHC1) has been designed and realized by the CERN RD-19 collaboration [16]. Its electronics features improved testability, better timing properties (LHC-oriented) and the lowest threshold setting is around 10 kV. In order to fully investigate the chip behavior for ISPA tube applications, a complete electronic read-out system has been set up. At present, the detector chip is under test with radioactive sources emitting low-energy gamma rays.

In collaboration with DEP, the encapsulation of an LHC1 chip in a 40:11 mm demagnifying tube is already in progress. The anode has been designed and is under construction. The overall tube design is being optimized and a complete work package has been agreed upon.

In parallel, design geometries of 80:18 mm tubes with an anode comprising 4 LHC1 chips are under extensive discussion. A schematic layout of the focussing electrodes to provide the necessary defocussing factor of ~ 4 is shown in Fig. 17. Finally, discussions are in progress with the RD-19 collaboration to understand whether some of the specific

LHC-B requirements can be incorporated into a future chip, such as short readout times, square pixels and a few bits per pixel for the signal discrimination and digitization.

4.4 Prototype RICH

As described above, the two RICH detectors of LHC-B provide π/K separation over the momentum range 1–150 GeV/c. Three radiators are required, aerogel and C_4F_{10} gas upstream of the spectrometer magnet, and CF_4 in the downstream RICH. The upstream RICH combines the use of both aerogel and gas radiators, and a prototype has been designed to demonstrate its feasibility.

The aims of the prototype experimental programme are:

1. To perform a *system demonstration* in a charged particle beam, using HPD's to detect simultaneously the Cherenkov rings from the gas and the aerogel radiators.
2. To evaluate the performance of commercial HPD's: the single-photon sensitivity, the spatial precision and the signal/noise ratio.
3. To demonstrate the read-out of HPD's at LHC speed.
4. To measure the effects due to particles traversing the HPD's.
5. To study the Rayleigh scattering in the radiators using UV filters.
6. To evaluate mirror construction technologies.

4.4.1 Commercial Hybrid Photodetectors

HPD's with a 7-pixel anode are commercially available from DEP. In October 1996 DEP supplied 25-pixel HPD's for the CMS HCAL project. These HPD's have a 5×5 array of $3.5 \times 3.5\,\mathrm{mm}^2$ pixels. To match the LHC-B spatial precision requirements we have contracted DEP to supply us with seven 61-pixel HPD's with an hexagonal array of $2 \times 2\,\mathrm{mm}^2$ pixels. Delivery is scheduled for April 1997 (with a guaranteed substitution of 25-pixel devices if this deadline is not achieved).

4.4.2 HPD read-out

The read-out system of the 7×61 HPD pixel channels will be similar to those used for silicon microstrip detectors. Since the signals resulting from photoelectrons in an HPD ($\sim 3000\,e^-$) are small we will begin our investigations using slow front-end electronics (Viking/VA3 chip) for optimal noise performance. Analogue signals from the VA3 chip will be processed using the AROMA module (developed for ATLAS silicon detector R&D) which runs in a VME DAQ system. Read out at LHC speed will be tested later, using fast amplifiers (e.g. FELIX) optimized for low noise performance.

With the exception of the hybrid, which carries the front-end chip and connects to the HPD pixel contacts, all components of the read-out chain are available. This hybrid will be designed and supplied by the RAL electronics group.

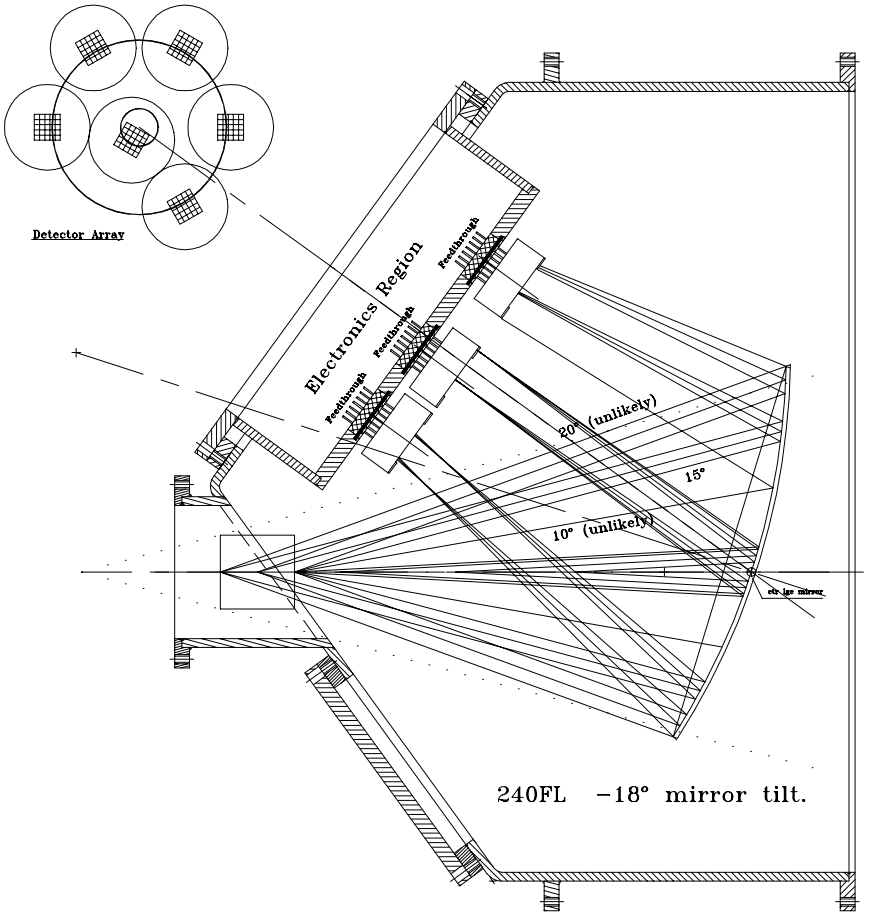

Figure 19: Layout 1 of the prototype RICH: a single tilted mirror of 240 mm focal length is used to focus rings from C_4F_{10} and aerogel simultaneously onto the detector plane (shown here as an array of 25-pixel HPD's).

4.4.3 Layout of prototype vessel and optics

The LHC-B RICH requirements will be tested using three layouts of the prototype. The different optical arrangements provide the following features:

1. Simultaneous detection of aerogel and gas rings using the *same* detector plane; this layout is illustrated in Fig. 19.

2. Full containment of aerogel and gas rings; an additional mirror of 120 mm focal length is used to contain the gas ring within a single HPD.

3. Measurement of ultimate spatial precision; a single tilted mirror of 1143 mm focal length is used to focus the ring from C_4F_{10} onto an array of 61-pixel HPD's; this layout is illustrated in Fig. 20.

Layouts 1 and 2 represent a 1/4 scale prototype of the LHC-B RICH, whereas Layout 3 is a full-scale prototype of the gas RICH system.

First tests will be performed using custom-built glass mirrors (orders already placed) to compare with subsequent tests of the light-weight mirror structures which will be required in the LHC-B RICH detectors.

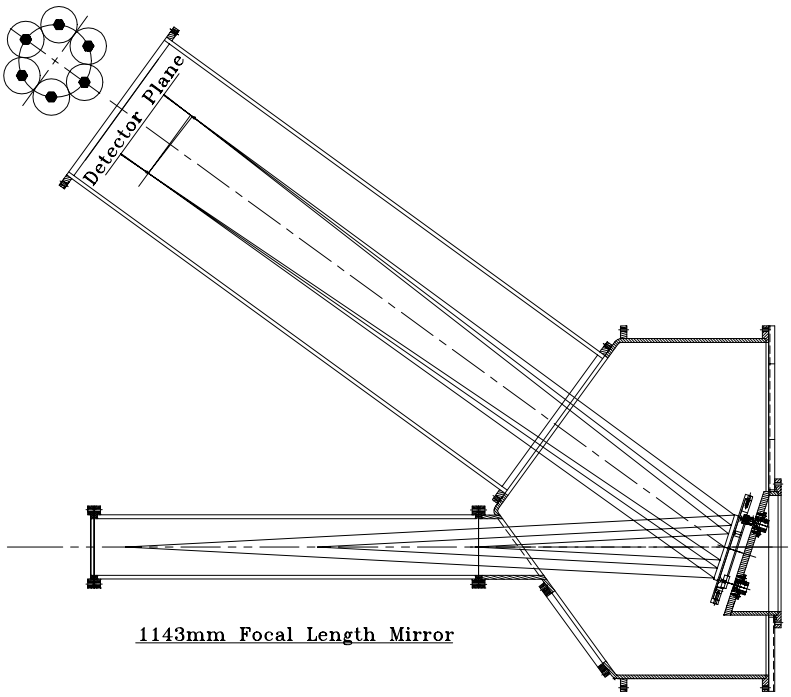

Figure 20: Layout 3 of the prototype RICH: extension pieces are added to permit the measurement of the ultimate spatial precision, in a full-scale prototype of the gas RICH.

4.4.4 Gas system

The purity of the fluorocarbon gas radiator, which has been an important consideration in previous RICH detectors (e.g. DELPHI), is related to absorption of wavelengths below $\sim 200\,\mathrm{nm}$. This is less critical for our application. The HPD spectral sensitivity ranges from 220–650 nm and a simple gas recirculation system, using molecular sieves or Oxysorb treatment, will be adequate.

4.4.5 Alternative photon detectors

The prototype vessel has been designed to allow testing of photon detectors other than the commercial HPD's. We envisage mounting and testing the ISPA tube and the "in-house" pad HPD, described earlier. The multianode photomultiplier, as proposed for the HERA-B RICH detector, will also be tested. A high quantum efficiency Gas Microdot Photodetector has been demonstrated to work successfully in the laboratory [17]. We intend to investigate its performance, with a CsI photocathode, to detect Cherenkov light in our RICH prototype.

4.4.6 Institute responsibilities

Engineering and assembly of prototype:	Imperial College
Optics and gas system:	Oxford
Read-out and DAQ:	Cambridge, Oxford
HPD development:	CERN, College de France
HPD evaluation:	Glasgow
Gas microdot photodetector:	Liverpool

5 Organization

The convener of the RICH working group is T. Ypsilantis (Collège de France). The people (and their institutes) involved in the various aspects of R&D are as follows:

Simulation

R. Forty, G. Wilkinson (CERN)
M. Tobar-Vidal (University of Santiago de Compostela)
L. Di Ciaccio (University of Rome "Tor Vergata")
N. Brook, A. Halley (University of Glasgow)

Aerogel

M. Alemi, R. Forty (CERN)
J. Seguinot, T. Ypsilantis (Collège de France)
C. Matteuzzi (University of Milan)
in collaboration with colleagues from University of Bari, University of Lecce and University of Rome "Sanità".[4]

Pad HPD

A. Braem, E. Chesi, P. Martinengo, E. Rosso, P. Weilhammer, P. Wicht (CERN)
J-P. Jobez, J. Seguinot, T. Ypsilantis (Collège de France)
in collaboration with colleagues from University of Bari and University of Rome "Sanità", and the authors of Ref. [15].

Pixel HPD

M. Campbell, T. Gys, E. Heijne, E. Rosso, W. Snoeys (CERN)
in collaboration with RD-19 and DEP.

Prototype

V. Gibson, C.P. Ward, S. Wotton (University of Cambridge)
R. Forty, T. Gys, T. Ruf, G. Wilkinson (CERN)
J. Seguinot, T. Ypsilantis (Collège de France)
N. Brook, A. Halley (University of Glasgow)
T. Bowcock, P. Hayman (University of Liverpool)
G. Barber, A. Duane, D. Websdale (Imperial College London)
J. Bibby, N. Harnew, F. Harris, J. Holt (University of Oxford)

This list includes only those with substantial involvement, and does not include technicians; it corresponds to approximately 20 full-time equivalent physicists and engineers.

[4] E. Cisbani, R. De Leo, S. Frullani, F. Garibaldi, M. Iodice, L. Lagamba, A. Leone, V. Manzari, E. Nappi, R. Perrino, T. Scognetti and G.M. Urciuoli.

6 Milestones

Concerning the key issues for R&D that were discussed in Section 1.2, the work required for the study of aerogel has largely been completed already. The remaining issue is the development of a suitable photodetector, and as discussed above the HPD is our preferred solution.

We believe that the crucial step is to demonstrate the feasibility of producing a large HPD, with diameter $\mathcal{O}(10\,\mathrm{cm})$. Large size is the key to achieving sufficient active-area coverage, as the inactive area is typically confined to the peripheral region of the device, and becomes fractionally less as the total area increases. Large size is also the key to reducing the cost per channel, as many more channels are incorporated in an individual device (for a given granularity) and the cost of increasing the number of pads or pixels on the silicon detector surface is small.

We therefore set as our primary milestone (to be achieved before submitting a Technical Proposal) the production of a large HPD, encapsulated in a vacuum vessel, with the required detector granularity. As has been discussed above, we are pursuing two approaches to the development of such a photodetector, the "pad" or "pixel" devices. Both lines of R&D aim to achieve this milestone by the end of 1997, and the choice between the two will be taken after this phase of R&D is complete.

These first prototypes will not be equipped with the electronics chips that will be ultimately required for operation at the LHC. Most of the issues to be addressed in producing a large HPD, such as the encapsulation under vacuum, and compatibility of photocathode and silicon technologies, are not directly affected by the read-out chip that is used. However, in parallel with the HPD prototype development we intend to demonstrate the feasibility of a obtaining a suitable high-speed electronics chip, which can be included within the HPD at a later stage.

A summary of the R&D plan is given in Fig. 21, in the form of a time chart.

References

[1] "Status of research and development activities for the LHC-B experiment", CERN/LHCC 96–30.

[2] "Research and development programme for the LHC-B experiment", CERN/LHCC 96–1.

[3] LHC-B Letter of Intent, "A dedicated LHC collider beauty experiment for precision measurements of CP violation", CERN/LHCC 95–5.

[4] T. Ypsilantis and J. Seguinot, Nucl. Instr. and Meth. A **368** (1995) 229.

[5] D.E. Fields *et al.*, Nucl. Instr. and Meth. A **349** (1994) 431.

[6] S.K. Sahu *et al.*, "Measurement of radiation damage on silica aerogel Cherenkov radiator", BELLE/96-1, to appear in Nucl. Instr. and Meth. A.

[7] R. De Salvo *et al.*, Nucl. Instr. and Meth. A **315** (1992) 375.

[8] T. Ypsilantis and J. Seguinot, Nucl. Instr. and Meth. A **343** (1994) 30.

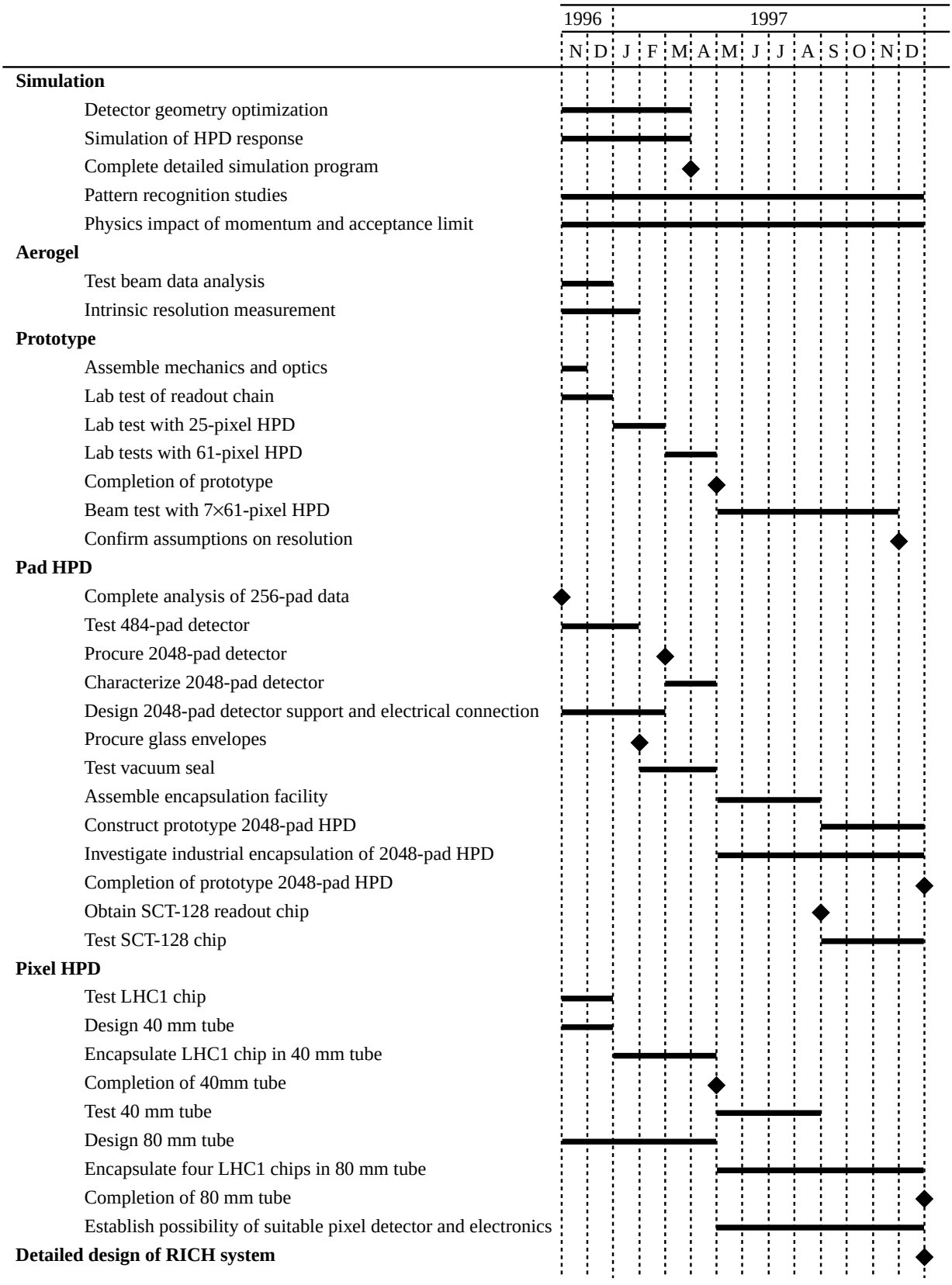

Figure 21: Time chart of the R&D plan, with milestones marked by diamonds.

[9] R.W. Forty, "Ring-imaging Cherenkov Detectors for LHC-B", LHC-B/96–05, presented at BEAUTY 96, to appear in Nucl. Instr. and Meth. A.

[10] E. Chesi *et al.*, "Performance of a 256-pad Hybrid Photon Detector for ring imaging", LHC-B/96–06, appended to this document.

[11] T. Gys *et al.*, Nucl. Instr. and Meth. A **355** (1995) 386.

[12] M. Campbell *et al.* (RD-19 collaboration), Nucl. Instr. and Meth. A **342** (1994) 52.

[13] T. Gys *et al.*, "Position-sensitive single-photon detection with a hybrid silicon pixel array tube", to appear in Proc. of 1st Conf. on Developments in Photodetection, Beaune (June 1996).

[14] T. Gys *et al.*, CERN technical note, in preparation.

[15] E. Chesi *et al.*, "Performance of silicon pad sensors for a RICH detector", LHC-B/96–07, appended to this document.

[16] E.H.M. Heijne *et al.*, "LHC1: A semiconductor pixel detector readout chip with internal, tunable delay providing a binary pattern of selected events", CERN–ECP/96–03, presented at Hiroshima Symposium (1995), submitted to Nucl. Instr. and Meth. A.

[17] S.F. Biagi and T.G. Jones, Nucl. Instr. and Meth. A **361** (1995) 72.